

A SPACE-BASED OBSERVATIONAL STRATEGY FOR CHARACTERIZING THE FIRST STARS AND GALAXIES USING THE REDSHIFTED 21-CM GLOBAL SPECTRUM

JACK O. BURNS¹, RICHARD BRADLEY⁶, KEITH TAUSCHER^{1,2}, STEVEN FURLANETTO³, JORDAN MIROCHA³, RAUL MONSALVE¹, DAVID RAPETTI^{1,9}, WILLIAM PURCELL¹³, DAVID NEWELL¹³, DAVID DRAPER¹³, ROBERT MACDOWALL⁴, JUDD BOWMAN⁵, BANG NHAN^{1,6}, EDWARD J. WOLLACK⁴, ANASTASIA FIALKOV⁸, DAYTON JONES¹¹, JUSTIN C. KASPER⁷, ABRAHAM LOEB⁸, ABHIRUP DATTA^{1,12}, JONATHAN PRITCHARD¹⁰, ERIC SWITZER⁴, MICHAEL BICAY⁹,

¹Center for Astrophysics and Space Astronomy, Department of Astrophysical and Planetary Science, University of Colorado, Boulder, CO 80309, USA

²Department of Physics, University of Colorado, Boulder, CO 80309, USA

³Department of Physics and Astronomy, University of California at Los Angeles, Los Angeles, CA 90095, USA

⁴NASA Goddard Space Flight Center, Greenbelt, MD 20771, USA

⁵Arizona State University, School of Earth and Space Exploration, P.O. Box 876004, Tempe, AZ 85287, USA

⁶National Radio Astronomy Observatory, 520 Edgement Road, Charlottesville, VA 22903, USA

⁷Department of Climate and Space Sciences and Engineering, University of Michigan, Ann Arbor, MI 48109, USA

⁸Center for Astrophysics, 60 Garden St., MS 51, Cambridge, MA 02138, USA

⁹NASA Ames Research Center, Moffet Field, CA 94035, USA

¹⁰Department of Physics, Blackett Laboratory, Imperial College, London SW7 2AZ, UK

¹¹Space Science Institute, 4750 Walnut Street, Suite 205, Boulder, CO 80301, USA

¹²Indian Institute of Technology, Indore, India and

¹³Ball Aerospace Corporation, 1600 Commerce Street, Boulder, CO 80301 USA

Draft version April 11, 2017

ABSTRACT

The redshifted 21-cm monopole is expected to be a powerful probe of the epoch of the first stars and galaxies ($10 < z < 35$), never before observed. This hyperfine transition of HI is sensitive to the thermal and ionization state of hydrogen gas and thus provides a tracer of sources of energetic photons – primarily hot stars and accreting black holes – which ionize and heat the high redshift intergalactic medium. Sky-averaged spectra of the redshifted 21-cm background are expected to exhibit broad absorption and emission features relative to the microwave background at low radio frequencies, ≈ 40 – 120 MHz. In a low altitude lunar orbit, night-time spectral observations while on the farside avoid terrestrial radio frequency interference, ionospheric corruption, and solar radio emissions. The distinctive frequency structure, uniformity over large scales, and unpolarized state of the redshifted 21-cm spectrum are distinct from the spectrally featureless, spatially-varying and polarized emission from bright Galactic foregrounds. This allows a clean separation between the primordial signal and foregrounds using Bayesian inference techniques such as Markov Chain Monte Carlo. We illustrate how this signal can be detected in the presence of foregrounds using the instrument parameters for the *Dark Ages Radio Explorer* (DARE), and to subsequently constrain the properties of the high- z intergalactic medium and the parameters of a simple first stars model.

Keywords: cosmology: dark ages, reionization, first stars - cosmology: observations

1. INTRODUCTION

One of the last frontiers of observational cosmology is the time period stretching from the end of the Dark Ages through Cosmic Dawn (≈ 80 – 500 million years after the Big Bang). This is a virtually unobserved yet key epoch in the early Universe. During this interval, the first luminous objects including stars, galaxies, and accreting black holes “turned on” (e.g., [Loeb & Furlanetto 2013](#)). Furthermore, this time period saw the birth of structural complexity in the Universe. At the beginning of the Dark Ages, corresponding to the Epoch of Recombination, the Universe was smooth to 1 part in 10^5 as evidenced by the Cosmic Microwave Background (CMB; e.g., [Mather et al. 2013](#)). Yet less than a billion years later, the Universe was teeming with complex structure spanning many orders of magnitude in scale. Thus, this transition time in the Universe is vital to understanding how the core components and structures of today’s Universe came to be.

The highly-redshifted 21-cm spectral line of neutral hydrogen, produced by a spin-flip hyperfine transition ([Field 1958](#)), provides an observable window into the early Universe’s intergalactic medium (IGM) before the Epoch of Reionization (EoR) was complete ([Madau et al. 1997a](#)). The heating and ionization caused by the “first objects to light up the Universe”¹ serve as indirect probes of the nature of the first stars and galaxies. With an effective optical depth of $\approx 1\%$ and sensitivity to low temperatures, the resulting signal measured against the CMB permits us to investigate a large evolutionary range from the Dark Ages through the end of the EoR (e.g., [Furlanetto et al. 2006](#); [Morales & Wyithe 2010](#); [Pritchard & Loeb 2012](#)).

The 21-cm all-sky or global signal ([Shaver et al. 1999](#); [Pritchard & Loeb 2010](#)) (Figure 1) is an attractive observational target for either a single antenna (e.g., [Bow-](#)

¹ NRC Astrophysics Decadal Survey: New Worlds, New Horizons in Astronomy and Astrophysics, <http://www.nap.edu/catalog/12951/new-worlds-new-horizons-in-astronomy-and-astrophysics>.

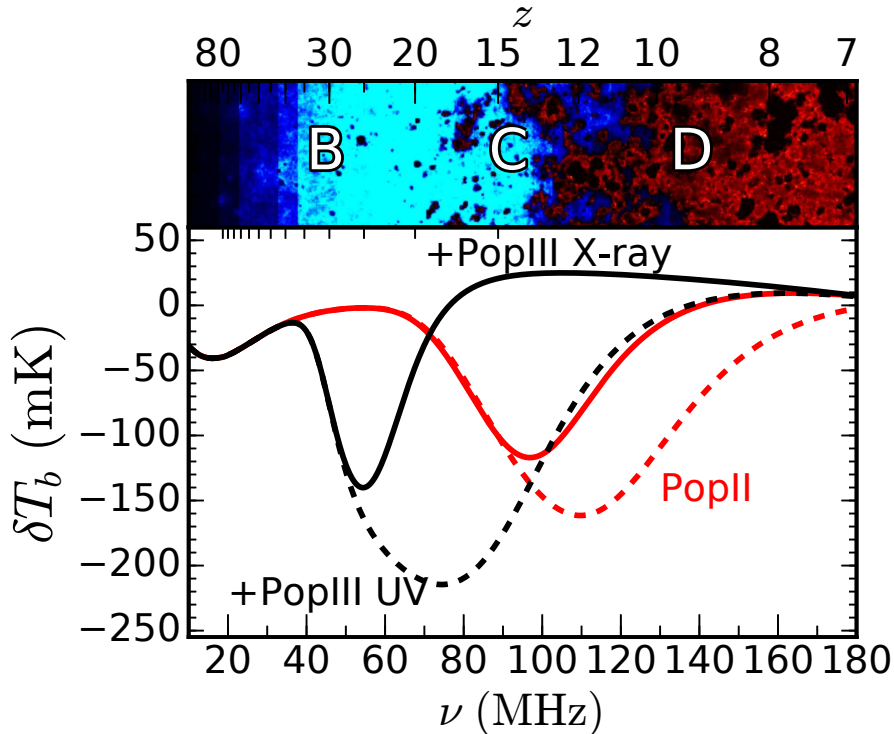


Figure 1. Shown here is the evolution of a slice of the Universe, from early times (left, upper panel) to late times (right) as well as several different models for the corresponding 21-cm spectrum relative to the CMB (lower panel). The red lines are conservative estimates with Pop II (metal-rich) stars only, while the black curves assume that Pop III (metal-free) star formation also occurs, but only in low-mass galaxies where atomic cooling is inefficient. The dashed and solid black curves assume that Pop III stars are distinct from Pop II stars in their emission properties – 100 times brighter in the UV (dashed) and in the UV + X-ray emissions (solid), respectively. The dashed red curve assumes stellar properties corresponding to low redshift Pop II stars whereas the solid red curve corresponds to metallicities of 5% solar. Designations B, C and D indicate the redshift corresponding to the ignition of first stars, the formation of initial black hole accretion, and the onset of reionization, respectively. See Section 6 for further discussion. Figure adapted from [Pritchard & Loeb \(2010\)](#) using the new reference models from [Mirocha et al. \(2017\)](#).

man & Rogers 2010; Burns et al. 2012; Patra et al. 2013; Voytek et al. 2014; Bernardi et al. 2015; Sokolowski et al. 2015a) or a small, compact array of antennas (e.g., Presley et al. 2015; Vedantham et al. 2015; Singh et al. 2015). Features in the spectrum may provide the first constraints on the birth and nature of the first luminous objects (e.g., Furlanetto 2006). Such an experiment for 21-cm cosmology is analogous to the COBE measurement of the CMB blackbody spectrum, which set the stage for more detailed studies of spatial fluctuations by WMAP and Planck.

In this paper, we describe how the 21-cm global signal can be used to place constraints on the time of formation and the characteristics of the first stars and galaxies. We demonstrate how signal extraction using a realistic radiometer system and Bayesian statistical techniques, in the presence of strong galactic and extragalactic foregrounds, can measure spectral features and constrain the physical properties of the first luminous objects.

We describe potential observations at low frequencies down to 40 MHz in an orbit around the Moon with data taken only above the lunar farside. On Earth, the ionosphere corrupts low frequency observations (see e.g., and references therein: Vedantham et al. 2014; Vedantham & Koopmans 2015; Rogers et al. 2015; Sokolowski et al.

2015b; Datta et al. 2016) due to refraction, absorption, and emission driven by solar emissions and the solar wind (Davies 1990; Liu et al. 2011; Polygiannakis et al. 2003). At 50 km above the lunar farside, we calculate that >90 dB of radio frequency interference (RFI) attenuation produces an environment quiet to <1 mK (e.g., McKinley et al. 2013). In addition, the Moon shields the instrument (about half the time) from variable solar emission caused by flares and coronal activity (e.g., Mercier & Trotter 1997). Therefore, observations above the nighttime, pristine, radio-quiet lunar farside (as verified by RAE-2, Alexander & Kaiser 1976) bypass the challenges presented by the Earth and the Sun and provide an optimal site for measurements of the global 21-cm signal.

The key insight permitting Cosmic Dawn to be detected in the presence of bright foregrounds is that once the Moon blocks solar effects and terrestrial RFI, the foregrounds are significantly different in their characteristics from the expected 21-cm spectral signal. The 21-cm monopole strength is much weaker than the Galactic foreground ($T_{21\text{cm}}/T_{\text{foreground}} < 10^{-4}$). However, the 21-cm signal is separable from the foreground because it is spatially uniform at angular scales $\gtrsim 10^\circ$ (e.g., Bitner & Loeb 2011; Liu et al. 2013), unpolarized, and has distinct spectral features whereas the foreground varies

spatially, exhibits polarized emission, and is spectrally featureless. The 21-cm cosmological signal can then be extracted using algorithms similar to those employed for CMB observations implemented via a Markov Chain Monte Carlo framework (Harker et al. 2012, 2016).

This paper is organized as follows. In Section 2, an overview of the expected sky-averaged 21-cm signal is presented. Section 3 describes the nature and brightness of astronomical foregrounds which must be considered in efforts to measure the much weaker Cosmic Dawn signal. Section 4 provides a synopsis of a specific, realistic instrument that is currently proposed to observe the 21-cm monopole from the Moon. The updated design instrument parameters for the *Dark Ages Radio Explorer* (DARE; Burns et al. 2012) are used to illustrate how the 21-cm spectrum can be separated from the astronomical foreground. Section 5 describes our software pipeline for signal extraction using Bayesian statistical methods. In Section 6, we discuss the physical parameters (and their uncertainties) associated with the first stars, black holes, and galaxies that are expected to be measured using the 21-cm all-sky spectrum. Section 7 presents a summary of the potential use of the 21-cm background to detect the first luminous objects in the early Universe.

2. OVERVIEW OF THE 21-CM GLOBAL SIGNAL

The 21-cm global signal arises from the radiation effects produced by the first stars, accreting black holes, and galaxies on the surrounding IGM. X-ray and UV emission from these objects and their descendants heated and ionized the tenuous gas that lies between galaxies, culminating in the Epoch of Reionization several hundred Myrs later. The 21-cm background can be used to measure these radiation effects with the hyperfine line of the neutral hydrogen (HI) gas pervading the Universe. The expansion of the Universe redshifts these photons from earlier epochs to lower observed frequencies, $\nu = 1420/(1+z)$ MHz (e.g., at $z = 30$, $\nu = 45$ MHz). Importantly, this frequency-redshift relation enables a direct reconstruction of the history of the Universe as a function of time from the 21-cm spectrum, a powerful tool that is largely independent of detailed theoretical assumptions.

Figure 1 shows some example predictions (amongst those currently allowed) for the 21-cm spectrum during the Dark Ages and Cosmic Dawn. The brightness temperature of this 21-cm signal is given by (e.g., Madau et al. 1997b; Shaver et al. 1999; Furlanetto et al. 2006)

$$\delta T_b \simeq 27 x_{\text{HI}} \left(\frac{T_s - T_{\text{CMB}}}{T_s} \right) \left(\frac{1+z}{10} \right)^{1/2} (1 + \delta_B) \left[\frac{\partial_r v_r}{(1+z)H(z)} \right]^{-1} \text{ mK}, \quad (1)$$

where x_{HI} is the fraction of neutral gas, T_s is the 21-cm spin temperature, T_{CMB} is the CMB temperature, δ_B is the baryon overdensity (taken here to be $\delta_B \sim 0$), and $H(z)$ is the Hubble parameter. The last term in this equation includes the effect of the peculiar velocities with line of sight velocity derivative $\partial_r v_r$. The effects of the last term in Equation 1 are negligible for observations of the sky-averaged global signal (e.g., Bharadwaj & Ali

2004; Barkana & Loeb 2005).

Several important physical processes drive the evolution of δT_b with redshift. These include: (1) UV radiation from the first stars, which “activates” the spin-flip signal through the Wouthuysen-Field mechanism (Wouthuysen 1952; Field 1958); (2) X-ray heating, likely generated by gas accretion onto the first black holes; and (3) ionizing photons from the first galaxies (which destroy the neutral hydrogen).

The relevant radiation backgrounds grow at different times, so their interplay creates distinct features in the spectrum (Furlanetto et al. 2006; Pritchard & Loeb 2010; Mesinger et al. 2011). When the first stars appear ($z \sim 35 - 22$ across our range of models; Region B in Figure 1), their UV radiation drives T_s toward the cold temperatures that are characteristic of IGM gas, triggering a deep absorption trough (Madau et al. 1997a). Shortly after, black holes likely formed ($z \sim 25 - 12$ across our range of models; Region C), e.g., as remnants of the first stars. The energetic X-ray photons from these accreting black holes travel great distances, eventually ionize H and He atoms, and produce photo-electrons that deposit their energy largely as heat in the IGM (Shull & van Steenberg 1985; Furlanetto & Johnson Stoeber 2010), transforming the 21-cm signal from absorption into emission as the gas becomes hotter than the CMB (Region D). The emission peaks as photons from these stars and black holes ionize the IGM gas ($z < 12$), eventually eliminating the spin-flip signal.

The dashed red curve in Figure 1 assumes that the efficiency and properties of star formation in early galaxy populations (Sun & Furlanetto 2016; Mirocha et al. 2017) and the relationship between X-ray luminosity and star formation rate are the same as at later times (Mineo et al. 2012). There are several reasons to expect that this Pop II model is conservative. For example, it assumes solar metallicity, though stars in high- z galaxies are likely forming in metal-poor environments, which can boost their UV (Eldridge & Stanway 2009) and X-ray outputs (Borby et al. 2016). The solid red curve in Figure 1 assumes that galaxies have metallicities (Z) 5% of solar, which results in a shallower absorption feature due to enhanced X-ray emission (assuming the Borby et al. 2016 L_X -SFR- Z relation). Alternatively, the black curves include a simple model for Pop III stars, in which low-mass halos (below atomic cooling threshold) can produce UV and X-ray photons (neglected by red curves). Boosts of 100 in the efficiency of the UV (dashed black) and also the X-ray luminosity (solid black) of Pop III stars relative to Pop II result in a variety of qualitatively different predictions for the global 21-cm signal. Pop III models that resemble our black curves should be relatively straightforward to distinguish from Pop II-only models for an experiment like DARE (see Section 4 and Figure 6). At this stage, our ability to label each set of curves as being Pop II- or Pop III-dominated assumes that the current Pop II models are well calibrated (Mirocha et al. 2017). New measurements (by e.g., JWST) in the coming years can be immediately incorporated into the model, and will act to mitigate degeneracies between Pop II and Pop III sources. More subtle features of the signal, such as its asymmetry, may also reveal the presence of Pop III despite uncertainties in the calibration of Pop II models (Mirocha et al., in preparation).

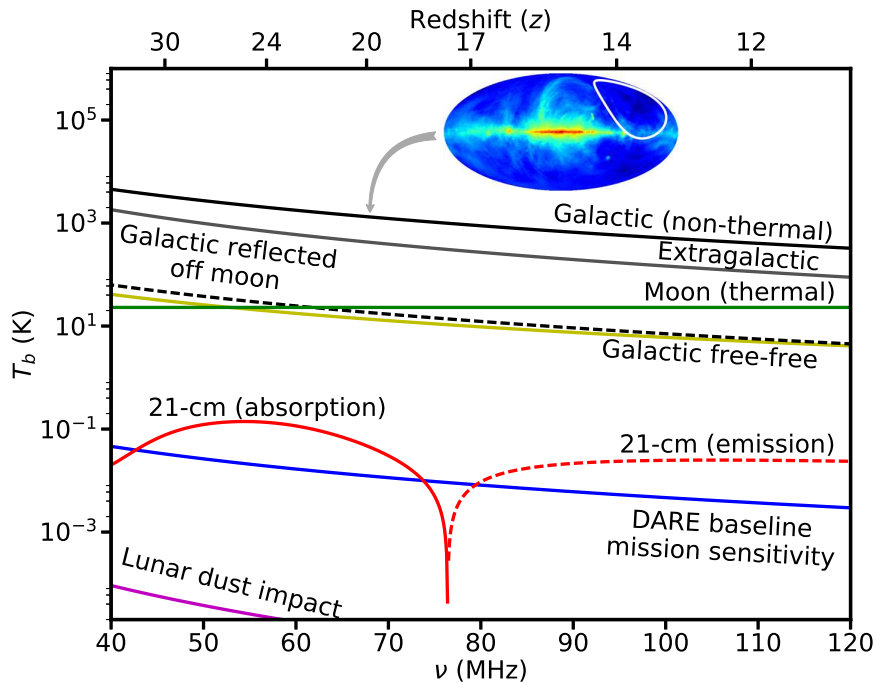


Figure 2. The Galactic and Extragalactic spectra are shown for a typical region away from the Galactic center. The Galaxy spectrum also reflects off the Moon (Evans 1969). The Moon’s thermal emission at low radio frequencies arises from cold, uniform subsurface layers. The effects of hyperkinetic dust impacts on the spacecraft in orbit of the Moon are unimportant. The red curve illustrates the spectral features in the 21-cm spectrum, where the dashed part of the curve corresponds to emission and the solid to absorption for this log-linear plot. *Insert:* A Mollweide projection of the sky at 408 MHz (Haslam et al. 1982) is shown along with a DARE beam FWHM white contour.

It is also worth noting that the 21-cm global signal traces the collective effects of all sources in the redshift ranges illustrated in Figure 1, which form a mostly unresolved sea of fainter objects that likely dominate the total emissivity of the early Universe. The red curves in Figure 1 are calibrated to match the latest luminosity function measurements from HST (which probe relatively bright galaxies that can be resolved) and CMB optical depth (τ_e) measurements from Planck (Mirocha et al. 2017), with variations arising solely due to differences in the adopted properties of galaxies beyond the current detection threshold. JWST and future CMB missions will further constrain the bright-end of the galaxy luminosity function and τ_e , respectively, and will thus enhance the sensitivity of the 21-cm global signal to Pop III stars and their remnants in faint galaxies.

3. FOREGROUNDS

3.1. Galaxy/Extragalactic Foregrounds

Beam-averaged diffuse sky foregrounds represent the strongest contributors to the 21-cm measurement for a space-based experiment. The most important arises from our Galaxy (Shaver et al. 1999). In addition, a “sea” of Extragalactic sources appear as another diffuse, spectrally-featureless power-law foreground (at DARE’s resolution) and contributes $\sim 10\%$ of the total sky brightness temperature (Figure 2). The emission from these foregrounds is produced by synchrotron radiation that intrinsically has a smooth frequency spectrum (e.g., Bernardi et al. 2015; Petrovic & Oh 2011).

Theoretical models predict that the foreground is well

approximated by a third-order polynomial to levels below the amplitude of the 21-cm global signal, especially over low-foreground regions (Bernardi et al. 2015). Smoothness over a frequency range much broader than ~ 40 -120 MHz is supported by sky models produced from measurements that cover the range 10 MHz - 5 THz (de Oliveira-Costa et al. 2008; Zheng et al. 2017; Sathyanarayana Rao et al. 2017). These models rely on, at most, five components to describe the spectral content of the foreground over several decades in frequency. Global measurements from the Experiment to Detect the Global EoR Signature (EDGES), Sonda Cosmológica de las Islas para la Detección de Hidrógeno Neutro (SCI-HI), Shaped Antenna measurement of the background Radio Spectrum (SARAS), and Large-Aperture Experiment to Detect the Dark Ages (LEDA) provide further validation of the intrinsic foreground smoothness (Rogers & Bowman 2008; Mozdzen et al. 2017; Voytek et al. 2014; Patra et al. 2015; Bernardi et al. 2016).

On top of the spectral smoothness, the foregrounds are spatially variable (inset in Figure 2). Their featureless spectrum and spatial variability contrast with the spectral features and spatial uniformity of the 21-cm spectrum, making them separable (Liu et al. 2013; Switzer & Liu 2014). This is achieved by our signal extraction pipeline (see Section 5), which also includes spatial variations of the spectral index in the range constrained by current observations.

The spectrally featureless foreground is altered via the frequency-dependent antenna response (Vedantham et al. 2014; Bernardi et al. 2015; Mozdzen et al. 2016). The beam directivity of finite-sized, wideband anten-

nas does not remain constant across frequency (Rumsey 1966). This beam “chromaticity” impacts the observed spectrum of the spatially-dependent foregrounds. The variation with frequency of the beam shape and directivity imprints spectral structure into the beam-averaged response that is not intrinsic to the foregrounds. Chromaticity is addressed utilizing methods developed by ground-based instruments, both minimizing instrumental design effects and making precise beam measurements on the ground and on-orbit (see Section 4). Systematic effects will be further reduced via polarization measurements of the foreground, and use of an advanced signal extraction pipeline (see Section 5).

3.2. Polarization of the Foreground

Both intrinsic polarization (Jelić et al. 2014, 2015; Lenc et al. 2016) and induced polarization (instrumental or polarization leakage; Asad et al. 2015) are present in the foreground. We focus on the induced polarization to further distinguish the foreground from the unpolarized HI signal (see Section 4 and Nhan et al. 2017). Our observation strategy incorporates rotation about the bore-sight axis, both to average down intrinsic polarization effects and to modulate the induced polarization captured by the two polarization arms of the antenna. This modulation results in polarization that tracks and measures structure in the beam-averaged foreground spectrum, without relying on e.g., polynomial model fits, and is insensitive to the spatially uniform 21-cm signal. CMB polarization measurements use analogous modulation approaches, achieving stability and systematic control required for μK polarimetric sensitivity (e.g., Bennett et al. 2003; Bischoff et al. 2013).

3.3. Other Foregrounds

21-cm cosmology experiments in lunar orbit will also detect emission from the Moon via the antenna back-lobe. The lunar spectrum is comprised of (1) thermal emission from a ~ 100 m subsurface layer (i.e., electrical skin depth of the regolith) (Salisbury & Fernald 1971; Keilm & Langseth 1975) and (2) reflected Galactic emission, requiring a parameter in the data analysis pipeline to describe the Moon’s reflectivity (Davis & Rohlfs 1964; Vedantham et al. 2015).

Other processes have a minor effect on the spectrum. Hyperkinetic impacts of dust from the interplanetary medium and the lunar exosphere on the spacecraft surface generate radio transients (e.g., Meyer-Vernet 1985); but the dust distribution around the Moon (e.g., Stubbs et al. 2010), the capacitance of the spacecraft, and solar wind conditions produce most of its emission at frequencies < 40 MHz (Figure 2; Le Chat et al. 2013).

Bright, transient, nonthermal emission from Jupiter and Io also occur at < 40 MHz (Panchenko et al. 2013; Cecconi et al. 2012); however, at 40-120 MHz, the antenna temperature observed by an instrument like that proposed for DARE is only ~ 1 mK for Jupiter (Zarka 2004). Jupiter, and other astronomical sources such as Cas A (similarly beam-diluted), may introduce low-level spectral effects due to scattering off the spacecraft. Electromagnetic analysis, incorporating accurate models of the spacecraft, must be used to assess and calibrate these effects as part of the signal extraction pipeline.

Finally, carbon atoms in cold, diffuse gas in the Milky Way (and possibly in the IGM) produce radio recombination lines (RRLs; Peters et al. 2011; Morabito et al. 2014). These lines are sharp (~ 10 kHz wide), but spaced at known intervals of ~ 1 MHz. Spectral channels containing RRLs constitute a negligible fraction of the data and may be discarded. Removal of potential RRLs from the 21-cm spectrum will drive the spectral resolution of the science instrument. Also, beam dilution is expected to significantly reduce any impact from recombination lines.

4. THE DARE SCIENCE INSTRUMENT

To illustrate how the cosmological 21-cm spectrum can be extracted from the foreground, we use the science instrument proposed for DARE (Figure 3). A first generation instrument was outlined in Burns et al. (2012). The design for DARE has been significantly updated and continues under active development. Here, we describe the current state. The science instrument is being designed to provide data with the frequency range (40 – 120 MHz), spectral resolution (50 kHz), systematic uncertainty (≈ 17 mK residual RMS averaged across the spectral band), beam characteristics ($\approx 60^\circ$ FWHM at 60 MHz), and polarization required to measure the spectral features illustrated by the range of models in Figure 1. The expectation for the instrument envelopes the hardware performance of systems on the ground (e.g., EDGES, Bowman & Rogers 2010; Cosmic Twilight Polarimeter, CTP, Nhan et al. 2017) and in space (Global Precipitation Measurement Microwave Imager, GMI²). The beamwidth of the antenna provides a sampling of a large volume of the Universe in ≈ 4 sky pointings. The spectral resolution is sufficient to identify and remove Galactic radio recombination lines. The polarization capability is provided by orthogonal dipole antennas which will allow the generation of all 4 Stokes parameters and yield independent measurements of the foreground. The observations performed from the radio-quiet zone above the Moon’s farside, free of terrestrial interference, the Earth’s ionosphere, and solar emissions, will be enabled through a unique “frozen” 50×125 km lunar equatorial orbit (Plice et al. 2017).

Figure 4 shows a block diagram of the current DARE instrument design which consists of four subsystems: an antenna composed of a pair of crossed biconical dipoles above a ground plane that provides dual polarization with good reflection coefficient (-12 dB average across the band) and beam performance (beam directivity spectral knowledge goal is ~ 20 ppm, see below); a receiver with a thermally-controlled pilot frequency tone calibrated architecture optimized to provide a stable response that meets the RMS goal; a spectrometer with a wide bandwidth and digital receiver that provides the spectral resolution and Stokes processing of the V and H channels; and an instrument electronics subsystem to interface with the spacecraft.

The DARE thermal design is optimized to minimize temperature variations of the antenna and receiver by limiting exposure to the solar flux and lunar albedo. For the antenna, thermal baffles, as shown in Figure 3, result in a predicted antenna temperature change over the lunar

² <https://pmm.nasa.gov/gpm/flight-project/gmi>

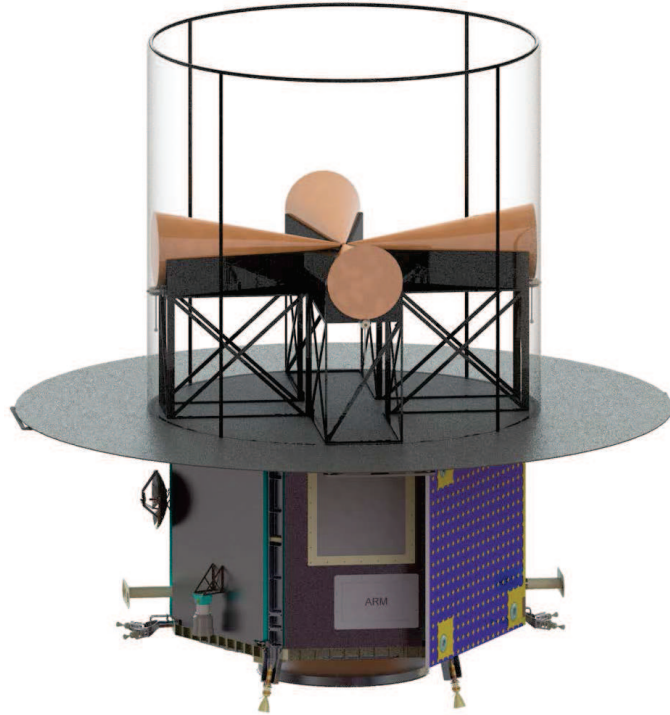


Figure 3. An artist rendering showing the DARE observatory. The science instrument thermal shield surrounds the antenna (shown transparent for clarity). The antenna consists of a pair of dual, crossed bicones. Beneath the antenna support structure is a deployed ground plane which aids in shaping the beam directivity. Below the instrument is the spacecraft bus including the solar panels and telemetry system.

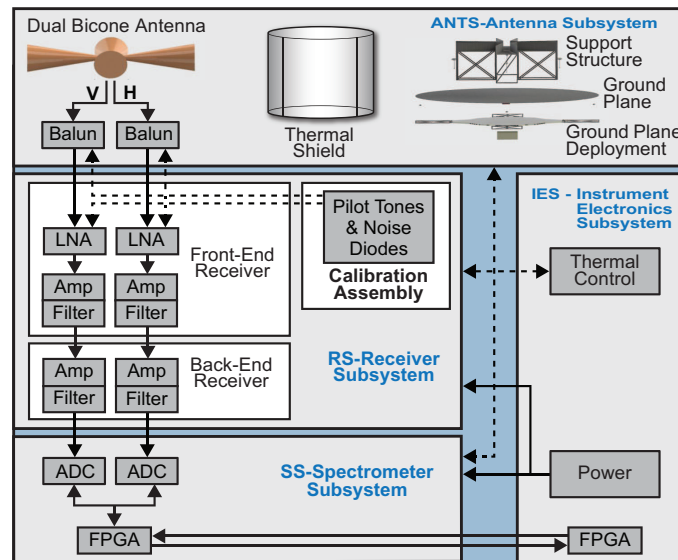


Figure 4. DARE instrument block diagram. DARE consists of four subsystems: dual polarization antenna, pilot tone calibration receiver and temperature control, high resolution digital spectrometer, and a standard instrument electronics module for power, data handling, and instrument control that interfaces with the spacecraft.

orbit of 10°C allowing DARE to maintain a nearly constant beam directivity. The front-end receiver includes a proportional-integral-derivative heater control to provide predicted thermal stability of 0.1°C , thus reducing receiver systematics to meet DAREs overall RMS noise and stability requirements.

A novel, new feature of the current DARE mission de-

sign is on-orbit calibration of the antenna directivity. Measurements of the beam will be obtained by receiving ≥ 3 narrow-band, circularly-polarized signals spaced across the band, transmitted from a large antenna on the Earth as DARE orbits the Moon above the nearside. The spacecraft (and antenna) is slowly rotated while it continuously receives these signals. The received signal

power at each frequency as a function of antenna pointing will produce a slice through the beam power pattern. The transmitted signals will also reflect off the lunar regolith and return to the same antenna on Earth to correct for ionospheric effects. The in-situ beam measurement system is currently being baselined to use the 140-foot radio telescope at the Green Bank Observatory, operating with 50% aperture efficiency, transmitting 10 kW of power, and using 10 second averaging.

Another innovation in the current design of DARE is polarization measurements to constrain the foreground. Power received from radio sources positioned off bore-sight, but within the field of view of the antenna, produce partially coherent signals at the terminals of the two orthogonal dipoles. Since the foreground sources are distributed asymmetrically about the field of view, an analysis of these signals yields an RF frequency dependent set of non-zero Stokes vectors that characterize the net projected polarization and total relative power spectral density of the sources. As the spacecraft revolves about the boresight while acquiring data, the composite Stokes vector is phase modulated, sweeping out a circle in Q,U-space at twice the angular rotation rate of the spacecraft. The resulting time-dependent, orthogonal sinusoids of Stokes Q and U parameters are phase-locked at each spectral channel to this fixed dynamical frequency, with amplitudes that trace the power spectral density of the foregrounds (Nhan et al. 2017). Importantly, the spatially isotropic 21-cm background produces no net polarized Stokes vector. This polarization modulation approach allows extraction of an unbiased measure of the foreground power spectral density.

5. EXTRACTING THE COSMIC 21-CM FEATURES

With the specific design characteristics for DARE described above, we can now present a realistic approach for extracting the 21-cm spectrum from the foregrounds as observed via this space-based instrument. We first outline our approach for instrument calibration and then discuss the signal extraction pipeline that we have developed.

5.1. Instrument Calibration

We model the forward instrument response following that used by EDGES (Monsalve et al. 2017) as:

$$P = g \left[|F|^2 (\eta T_A + (1 - \eta) T_{Ap}) (1 - |\Gamma_A|^2) + T_{off} \right], \quad (2)$$

where P is the raw power measured by the instrument, g and T_{off} represent the system gain and radiometric offset respectively, η accounts for the antenna and balun losses at physical temperature T_{Ap} , $1 - |\Gamma_A|^2$ accounts for the reflection coefficient of the antenna, and $|F|^2$ is the throughput of the receiver front end accounting for multiple reflections between the receiver and antenna. The instrument calibration activities consist of using ground, on-board and on-orbit calibration to invert the forward instrument response model and provide an estimate of the antenna temperature T_A .

During science observations, the receiver is calibrated continuously using the pilot tone injection receiver architecture. The calibration system generates tones at ≈ 5 frequencies simultaneously across the band to adequately

sample the frequency range. The tones are each within a single 50 kHz spectrometer bin, and thus produce negligible degradation in spectral performance. The nominal calibration cycle consists of a sequence of four states which are enabled for 10 seconds each: 1) high-level tones directed toward the receiver, 2) low-level tones directed toward the receiver, 3) high-level tones directed toward the antenna, and 4) low-level tones directed toward the antenna. The gain of the receiver is computed by differencing instrument-measured power from the high- and low-level injected tones toward the receiver divided by the difference in effective input brightness temperature of the tones characterized during pre-flight calibration. Likewise, the tones injected toward the antenna afford an on-board measurement of the antenna reflection computed in a similar fashion. The terms T_{off} , η , and $|F|^2$ are computed based on ground measurements and the on-orbit trending of the receiver gain and reflection coefficient.

5.2. Signal Extraction using an MCMC Approach

DARE's observing strategy utilizes ≈ 4 quiet-sky pointing directions away from the galactic center. For each sky direction, r , and calibration, DARE produces a spectrum of the antenna temperature, $T_{A,D}^{(r)}(\nu)$, where ν indicates the frequency channel. These spectra are then modeled as a linear combination of principal modes derived from Singular Value Decomposition (SVD) analyses (Switzer & Liu 2014; Paciga et al. 2013; Vedantham et al. 2014),

$$T_{A,M}^{(r)} = \sum_i (\lambda_{21})_i f_i(\nu) + \sum_j (\lambda_{sys})_j^{(r)} g_j(\nu). \quad (3)$$

The signal modes, $f_i(\nu)$, are derived from 10,000 realizations of the 21-cm spectrum created using a wide range of physical models³. The systematic modes $g_j(\nu)$ are derived from 10,000 simulations of the instrument and foreground systematics using Equation 2 and its inverse along with fiducial calibration and beam-weighted foreground parameters and their errors (Tauscher et al. in preparation). The instrument simulations account for all the identified uncertainties and priors, specifically for the ~ 20 ppm prior in the foreground assumed for induced polarization measurements. The beam-weighted foregrounds are described well by a polynomial of the form $T_{FG}(\nu) = T_0 \exp\left(\sum_i \theta_{FG,i}^{(r)} [\ln(\nu/\nu_0)]^i\right)$. By fitting the realizations of the foreground to T_{FG} with reference temperature $T_0 = 1$ K, we obtain a mean and covariance of θ_{FG} which are used in defining the priors for λ_{sys} . Currently, we utilize the first 6 principal modes in each SVD set because, individually, they fit our fiducial signal and systematic models to within the thermal noise level achieved through 800 hours of integration. When fit simultaneously, however, we find that the covariance between the signal and systematic modes dominates the total error budget (see Figure 6).

Our current signal extraction pipeline uses a Markov Chain Monte Carlo (MCMC) analysis significantly updated from our earlier work described in Harker et al.

³ This set of models was derived by randomly sampling the parameter space surveyed in Mirocha et al. (2017), with the addition of two parameters that describe the UV and X-ray photon production efficiency in minihalos (i.e., those with $T_{virial} < 10^4$ K).

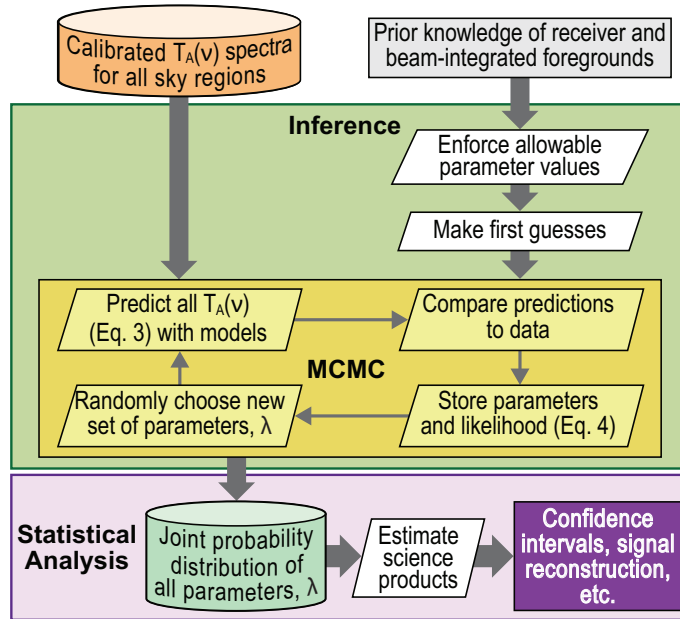


Figure 5. The 21-cm signal extraction pipeline simultaneously determines foreground, instrument, and 21-cm spectral parameters. From the calibrated T_A spectra, the MCMC extracts the signal (Figure 6) from which the values of the physical parameters are inferred (Figure 7). Prior knowledge of the receiver, beam, and foregrounds is exploited in making a first guess and in enforcing a parameter search that avoids regions of negligible likelihood. The MCMC numerically estimates the posterior probability distribution from which confidence intervals and signal reconstructions are calculated. In this diagram, parallelograms, cylinders, and boxes represent processes, data, and knowledge (input or output), respectively.

(2012, 2016). It separates the 21-cm spectrum from the foreground using the calibrated instrument measurements as detailed in the previous section. Using our nominal simulations, which assume 800 hours of effective sky integration, we combine the precisely measured antenna beam with the foreground information gleaned from polarization measurements and a linearized model for the remaining systematics resulting from T_A calibration. Our MCMC technique fits all model parameters simultaneously (using the EMCEE code; Foreman-Mackey et al. 2013) in order to account for the covariance between the parameters and ensure self-consistency. The Bayesian nature of the MCMC permits the incorporation of key prior knowledge on the instrument calibration and foregrounds when retrieving the posterior probability distribution of the model parameters. The MCMC method efficiently and robustly obtains the posterior distribution in the presence of bright foregrounds.

As shown in Figure 5, the MCMC pipeline samples the full parameter space, $\lambda = [\lambda_{sys}, \lambda_{21}]$, through an iterative process. On each iteration, the MCMC algorithm calculates the likelihood function

$$\ln L(\lambda) = -\frac{1}{2} \sum_r \sum_\nu \left[\frac{T_{A,D}^{(r)}(\nu) - T_{A,M}^{(r)}(\nu, \lambda)}{\sigma_r(\nu)} \right]^2, \quad (4)$$

where $T_{A,D}$ and $T_{A,M}$ are the antenna temperatures for the data and the model, respectively, and $\sigma_r(\nu) = T_{A,D}^{(r)}(\nu) / \sqrt{\Delta\nu \Delta t}$ is the statistical variance in the data for a given frequency channel ν of width $\Delta\nu$ and integration time Δt . By comparing the values of $\ln L(\lambda)$ for two successive sets of model parameters, the algorithm probabilistically determines whether to jump from the first to the second. By repeating this multiple times, the

MCMC sampler conducts a thorough and efficient walk that explores the parameter space λ . After convergence, the visited sets of parameters constitute a random sample from the posterior distribution, from which we can estimate the most likely values of the model parameters, as well as their confidence intervals and covariance.

For the DARE instrument parameters discussed in Section 4 and 800 hours of total integration above the lunar farside, our signal extraction pipeline predicts the recovered spectra and uncertainties for two representative models (Pop II and Pop III star models) shown in Figure 6. The MCMC pipeline simultaneously fits the receiver, beam, and foreground utilizing prior information and on-orbit measurements. Our instrument sensitivity metric is defined as the RMS uncertainty of the extracted spectrum averaged over the band. With an average RMS of ≈ 17 mK, we recover the major features in the spectra and differentiate between different stellar population models.

6. PHYSICAL PARAMETER ESTIMATION

With the calibrated spectra and uncertainties in Figure 6, it is straight-forward to estimate when the first luminous objects ignited and began reionizing the Universe. Since redshift maps directly to frequency, measurements of the extrema frequencies from the 21-cm spectrum determine when major events occurred in a mostly model-independent fashion (Harker et al. 2016). The frequency of the Region B extremum (ν_B) determines the z at which the UV background activates the 21-cm transition (i.e., first stars ignition). This clean and accurate measurement delineates the nature of the first stars, especially considering that no observational bounds currently exist. Using a Pop III model as a working example, DARE will extract ν_B with a 1% (0.4 MHz) uncertainty (68%

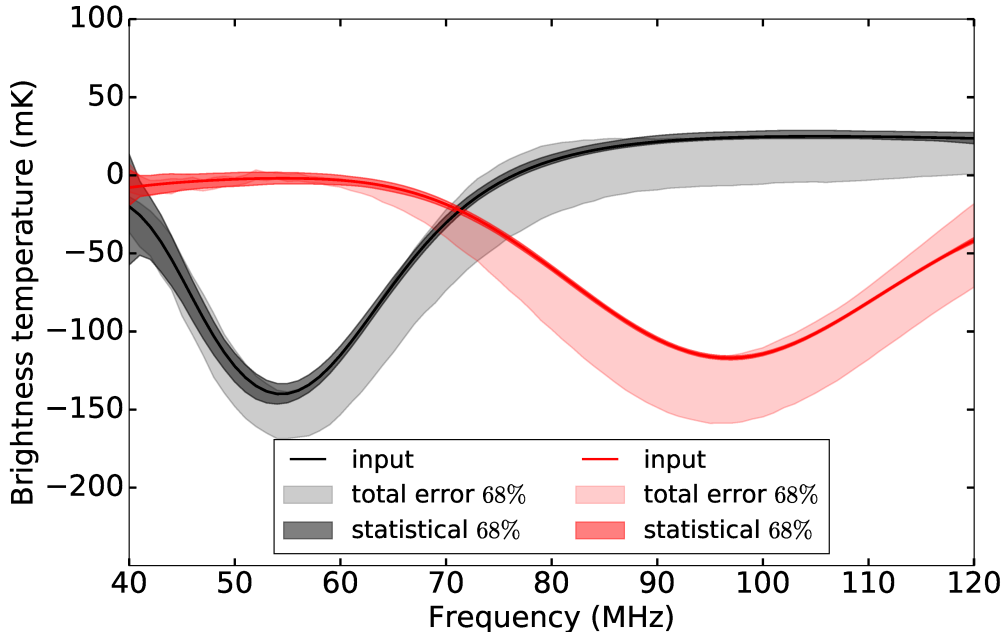


Figure 6. The extracted 21-cm spectra with 68% confidence intervals for models with primordial Pop II (red) and Pop III (black) stars expected using the DARE instrument parameters and 800 hours of observation. The dark bands represent thermal (statistical) noise from the sky. The total uncertainty, including statistical plus systematic errors from the instrument and foreground, are shown by the lighter bands, which are dominated by the covariance between the SVD signal and systematic modes.

confidence). Similarly, the redshift when the first black holes began accretion is measured from the Region C extremum frequency (ν_C) with 1% (0.6 MHz) uncertainty. The redshift of the beginning of reionization is measured from the extremum ν_D with 2% (2 MHz) uncertainty. Different models (Figure 1) yield similar uncertainties for the extrema frequencies.

The characteristics of the first stars and galaxies, along with the history of the early Universe, are determined from modeling of the calibrated spectrum. First, the history of reionization in the early Universe is characterized by the HI fraction (x_{HI}) and the IGM kinetic temperature (T_K) at $z \sim 11$. Our modeling of features in Region D using DARE’s sensitivity yields uncertainties of 5% and 10% for x_{HI} and T_K , respectively.

Next, the features in the 21-cm spectrum at the lowest frequencies depend upon the stellar populations that dominate the UV background; if, for example, Pop III star formation is efficient, we should expect features of the signal to occur at lower frequencies (higher redshift) than if Pop II stars dominate the background because Pop II stars form in more massive halos which do not become abundant until relatively late times (low redshift). DARE’s sensitivity can separate the effects of the broad classes of Pop II and Pop III stellar models considered in this work (see Figures 1 and 6), subject to the assumed calibration of the Pop II contribution (see Section 2; Mirocha et al. 2017) and the model for Pop III stars. A useful metric for gauging the influence of Pop III is the ratio of UV production efficiencies for Pop III compared to Pop II stars, $\xi_\alpha \equiv \xi_{\alpha,III}/\xi_{\alpha,II}$, which DARE constrains with 25% uncertainty (using the same Pop III model as shown in Figure 7).

The characteristics of the first X-ray sources (Region

C in Figure 1) are inferred from the ratio of X-ray heating efficiencies between Pop III and Pop II stars, ξ_X , which DARE can measure with 15% uncertainty (see Figure 7). Further modeling plus multi-wavelength observations (e.g., the cosmic X-ray background; Fialkov et al. 2017) may help to better constrain the identity of the Universe’s first X-ray sources, whether they be black hole X-ray binaries, hot gas in star-forming galaxies, or proto-quasars.

Finally, before concluding, we emphasize that these Pop III models are quite simple, as, for example, they neglect an explicit treatment of feedback. As a result, the interpretation of the precise value of $\xi_{\alpha,III}/\xi_{\alpha,II}$ may be considerably more complex in practice, but the finding that both values are non-zero is robust.

7. CONCLUDING REMARKS

To achieve the science potential of 21-cm global spectral observations, careful consideration must be given to the local environment, the instrument, and methods for signal extraction. A lunar-orbiting experiment above the Moon’s farside has the best probability of measuring the 21-cm spectrum since this environ is free of ionospheric effects and human-generated radio frequency interference.

Signal extraction in the presence of bright foregrounds is the greatest challenge for all observations of the 21-cm cosmological spectrum. Utilizing a Markov Chain Monte Carlo numerical inference technique, we showed that it is possible to accurately recover the frequencies and expected features in the spectrum in the presence of bright foregrounds with the instrument characteristics of the *Dark Ages Radio Explorer* (DARE) for ≈ 800 hrs of integration. To separate the signal from the fore-

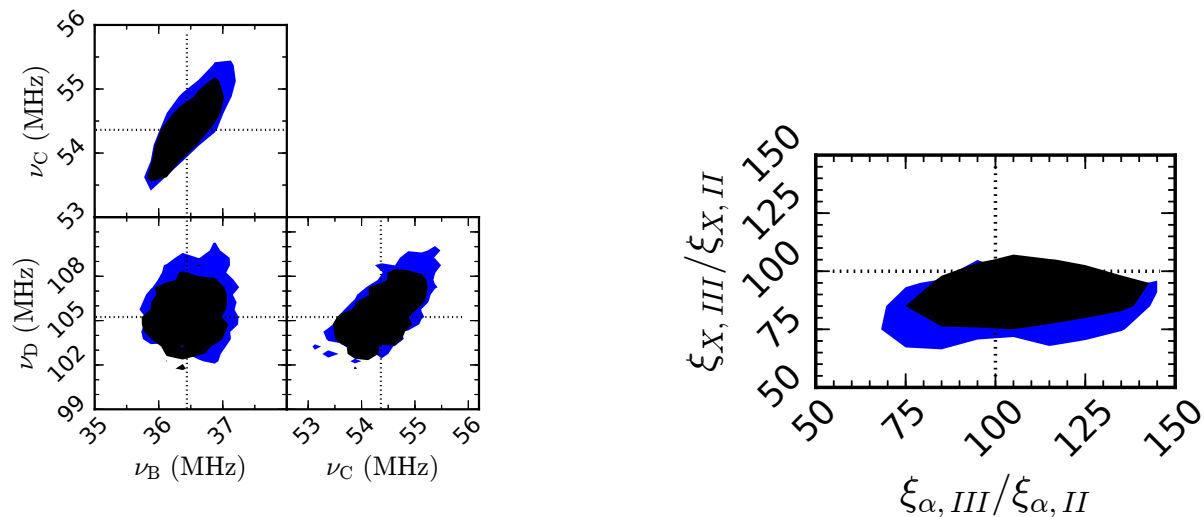


Figure 7. The panels illustrate examples of constraints on the global 21-cm extrema frequencies (left), UV photon production efficiency (ξ_α) and X-ray heating efficiency (ξ_X) between models with Pop III and Pop II stars (right) using the calibrated 21-cm spectrum. Dotted black lines indicate the “true” input values. These constraints assume RMS uncertainties in the 21-cm spectrum of 23 mK (black) and 30 mK (purple), which represent a performance margin above DARE’s design of 17 mK average RMS. The contours are at the 68% confidence intervals.

ground, the antenna system must be well-characterized requiring temperature control and precise beam directivity measurements on the ground and in-space. In addition, a model-independent constraint on the foreground from polarimetric observations is an important element in the signal extraction.

From the extracted 21-cm spectrum (including confidence intervals), we showed that meaningful constraints can be placed upon the physical parameters of primordial radiating objects. The redshift for the commencement of first star formation and X-ray emission from the first accreting black holes along with the redshift of the beginning of reionization can be inferred to within \approx a few percent. The 21-cm signal is also uniquely sensitive to the different radiation effects produced by Pop II and Pop III stellar models. Specifically, the UV production and X-ray heating efficiencies can be constrained, thus determining which stellar population was dominant within the first galaxies. Finally, the history of reionization in the early Universe can be characterized by the redshift evolution of the HI ionization fraction (x_{HI}) inferred from the 21-cm spectrum.

Accurate parameter estimation is a core capability required for 21-cm global signal observations and interpretations. Bayesian methods have significant potential for 21-cm observations (Greig et al. 2016; Bernardi et al. 2016). They have proven to be successful for other low signal-to-noise experiments including CMB observations (Planck Collaboration et al. 2016a,b) and the LIGO gravitational wave detections (Abbott et al. 2016; Veitch et al. 2015). The next step in the analyses of the global 21-cm spectrum to construct a likelihood function allowing differentiation between differing physical models for the first halos. Similarly, modeling different levels of structure in the beam-convolved foregrounds needs a

refined Bayesian approach. This is a highly computationally intensive process. However, recent developments of Nested Sampling algorithms for high dimensional parameter spaces which operate in massively parallel computer architectures (Handley et al. 2015) have great potential for 21-cm cosmology applications.

In conclusion, measurements of spectral features in the 21-cm spectrum will answer key science questions from the NRC Astrophysics Decadal Survey: “What were the first objects to light up the Universe and when did they do it?” With a clean measurement within the radio-quiet environs of the Moon’s farside and proven technology, the 21-cm global signal will open a new window of discovery into the early Universe.

This research was supported by the NASA Ames Research Center via grants NNA09DB30A, NNX15AD20A, and NNX16AF59G to JB, and by NASA ATP grant NNX15AK80G to SF and JB. DR is supported by a NASA Postdoctoral Program Senior Fellowship at the NASA Ames Research Center, administered by the Universities Space Research Association under contract with NASA. We thank the following colleagues for their important contributions including Jill Bauman, Jay Bookbinder, Matthew D’Ortenzio, Robert Hanel, Butler Hine, Stephanie Morse, Ken Galal, Laura Plice, Gary Rait, Jeremy Stober, and Eugene Tu. We also benefited from helpful conversations with James Aguirre, Mina Cappuccio, James Condon, Steven Ellingson, Bryna Hazelton, Danny Jacobs, Mark LaPole, Adam Lidz, John Mather, Harry Partridge, Aaron Parsons, Jonathan Pober, Greg Taylor, Greg Schmidt, and Sandy Weinreb.

REFERENCES

- Abbott, B. P., Abbott, R., Abbott, T. D., et al. 2016, *Physical Review Letters*, 116, 061102
- Alexander, J. K., & Kaiser, M. L. 1976, *J. Geophys. Res.*, 81, 5948
- Asad, K. M. B., Koopmans, L. V. E., Jelić, V., et al. 2015, *MNRAS*, 451, 3709
- Barkana, R., & Loeb, A. 2005, *ApJ*, 624, L65
- Bennett, C. L., Bay, M., Halpern, M., et al. 2003, *ApJ*, 583, 1
- Bernardi, G., McQuinn, M., & Greenhill, L. J. 2015, *ApJ*, 799, 90
- Bernardi, G., Zwart, J. T. L., Price, D., et al. 2016, *MNRAS*, 461, 2847
- Bharadwaj, S., & Ali, S. S. 2004, *MNRAS*, 352, 142
- Bischoff, C., Brizius, A., Buder, L., et al. 2013, *ApJ*, 768, 9
- Bittner, J. M., & Loeb, A. 2011, *J. Cosmology Astropart. Phys.*, 4, 38
- Bowman, J. D., & Rogers, A. E. E. 2010, *Nature*, 468, 796
- Brorby, M., Kaaret, P., Prestwich, A., & Mirabel, I. F. 2016, *MNRAS*, 457, 4081
- Burns, J. O., Lazio, J., Bale, S., et al. 2012, *Advances in Space Research*, 49, 433
- Cecconi, B., Hess, S., Hérique, A., et al. 2012, *Planet. Space Sci.*, 61, 32
- Datta, A., Bradley, R., Burns, J. O., et al. 2016, *ApJ*, 831, 6
- Davies, K. 1990, in *International Beacon Satellite Symposium 1990*, ed. J. R. Manzano, 153–157
- Davis, J. R., & Rohlfs, D. C. 1964, *J. Geophys. Res.*, 69, 3257
- de Oliveira-Costa, A., Tegmark, M., Gaensler, B. M., et al. 2008, *MNRAS*, 388, 247
- Eldridge, J. J., & Stanway, E. R. 2009, *MNRAS*, 400, 1019
- Evans, J. V. 1969, *ARA&A*, 7, 201
- Fialkov, A., Cohen, A., Barkana, R., & Silk, J. 2017, *MNRAS*, 464, 3498
- Field, G. B. 1958, *Proceedings of the IRE*, 46, 240
- Foreman-Mackey, D., Hogg, D. W., Lang, D., & Goodman, J. 2013, *PASP*, 125, 306
- Furlanetto, S. R. 2006, *MNRAS*, 371, 867
- Furlanetto, S. R., & Johnson Stoeber, S. 2010, *MNRAS*, 404, 1869
- Furlanetto, S. R., Oh, S. P., & Briggs, F. H. 2006, *Phys. Rep.*, 433, 181
- Greig, B., Mesinger, A., & Pober, J. C. 2016, *MNRAS*, 455, 4295
- Handley, W. J., Hobson, M. P., & Lasenby, A. N. 2015, *MNRAS*, 450, L61
- Harker, G. J. A., Mirocha, J., Burns, J. O., & Pritchard, J. R. 2016, *MNRAS*, 455, 3829
- Harker, G. J. A., Pritchard, J. R., Burns, J. O., & Bowman, J. D. 2012, *MNRAS*, 419, 1070
- Haslam, C. G. T., Salter, C. J., Stoffel, H., & Wilson, W. E. 1982, *A&AS*, 47, 1
- Jelić, V., de Bruyn, A. G., Mevius, M., et al. 2014, *A&A*, 568, A101
- Jelić, V., de Bruyn, A. G., Pandey, V. N., et al. 2015, *A&A*, 583, A137
- Keihm, S. J., & Langseth, M. G. 1975, *Icarus*, 24, 211
- Le Chat, G., Zaslavsky, A., Meyer-Vernet, N., et al. 2013, *Sol. Phys.*, 286, 549
- Lenc, E., Gaensler, B. M., Sun, X. H., et al. 2016, *ApJ*, 830, 38
- Liu, A., Pritchard, J. R., Tegmark, M., & Loeb, A. 2013, *Phys. Rev. D*, 87, 043002
- Liu, L., Le, H., Chen, Y., et al. 2011, *Journal of Geophysical Research (Space Physics)*, 116, A09307
- Loeb, A., & Furlanetto, S. R. 2013, *The First Galaxies in the Universe*, ISBN: 9780691144917, Princeton, NJ: Princeton University Press.
- Madau, P., Meiksin, A., & Rees, M. J. 1997a, *ApJ*, 475, 429
- , 1997b, *ApJ*, 475, 429
- Mather, J., Hinshaw, G., & Page, L. 2013, *Cosmic Microwave Background in Planets, Stars and Stellar Systems. Volume 6: Extragalactic Astronomy and Cosmology.*, ed. T. D. Oswalt & W. C. Keel, 609
- McKinley, B., Briggs, F., Kaplan, D. L., et al. 2013, *AJ*, 145, 23
- Mercier, C., & Trottet, G. 1997, *ApJ*, 474, L65
- Mesinger, A., Furlanetto, S., & Cen, R. 2011, *MNRAS*, 411, 955
- Meyer-Vernet, N. 1985, *Advances in Space Research*, 5, 37
- Mineo, S., Gilfanov, M., & Sunyaev, R. 2012, *MNRAS*, 426, 1870
- Mirocha, J., Furlanetto, S. R., & Sun, G. 2017, *MNRAS*, 464, 1365
- Monsalve, R. A., Rogers, A. E. E., Bowman, J. D., & Mozdzen, T. J. 2017, *ApJ*, 835, 49
- Morabito, L. K., Oonk, J. B. R., Salgado, F., et al. 2014, *ApJ*, 795, L33
- Morales, M. F., & Wyithe, J. S. B. 2010, *ARA&A*, 48, 127
- Mozdzen, T. J., Bowman, J. D., Monsalve, R. A., & Rogers, A. E. E. 2016, *MNRAS*, 455, 3890
- , 2017, *MNRAS*, 464, 4995
- Nhan, B. D., Bradley, R. F., & Burns, J. O. 2017, *ApJ*, 836, 90
- Paciga, G., Albert, J. G., Bandura, K., et al. 2013, *MNRAS*, 433, 639
- Panchenko, M., Rucker, H. O., & Farrell, W. M. 2013, *Planet. Space Sci.*, 77, 3
- Patra, N., Subrahmanyan, R., Raghunathan, A., & Udaya Shankar, N. 2013, *Experimental Astronomy*, 36, 319
- Patra, N., Subrahmanyan, R., Sethi, S., Udaya Shankar, N., & Raghunathan, A. 2015, *ApJ*, 801, 138
- Peters, W. M., Lazio, T. J. W., Clarke, T. E., Erickson, W. C., & Kassim, N. E. 2011, *A&A*, 525, A128
- Petrovic, N., & Oh, S. P. 2011, *MNRAS*, 413, 2103
- Planck Collaboration, Ade, P. A. R., Aghanim, N., et al. 2016a, *A&A*, 594, A13
- Planck Collaboration, Adam, R., Aghanim, N., et al. 2016b, *A&A*, 596, A108
- Plice, L., Galal, K., & Burns, J. O. 2017, *ArXiv e-prints*, arXiv:1702.00286
- Polygiannakis, J., Preka-Papadema, P., & Moussas, X. 2003, *MNRAS*, 343, 725
- Presley, M. E., Liu, A., & Parsons, A. R. 2015, *ApJ*, 809, 18
- Pritchard, J. R., & Loeb, A. 2010, *Phys. Rev. D*, 82, 023006
- , 2012, *Reports on Progress in Physics*, 75, 086901
- Rogers, A. E. E., & Bowman, J. D. 2008, *AJ*, 136, 641
- Rogers, A. E. E., Bowman, J. D., Vierinen, J., Monsalve, R., & Mozdzen, T. 2015, *Radio Science*, 50, 130
- Rumsey, V. 1966, *Frequency Independent Antennas*, Academic Press, Electronic Science Series, New York.
- Salisbury, W. W., & Fernald, D. L. 1971, *Journal of the Astronautical Sciences*, 18, 236
- Sathyanarayana Rao, M., Subrahmanyan, R., Udaya Shankar, N., & Chluba, J. 2017, *AJ*, 153, 26
- Shaver, P. A., Windhorst, R. A., Madau, P., & de Bruyn, A. G. 1999, *A&A*, 345, 380
- Shull, J. M., & van Steenberg, M. E. 1985, *ApJ*, 298, 268
- Singh, S., Subrahmanyan, R., Udaya Shankar, N., & Raghunathan, A. 2015, *ApJ*, 815, 88
- Sokolowski, M., Tremblay, S. E., Wayth, R. B., et al. 2015a, *PASA*, 32, 4
- Sokolowski, M., Wayth, R. B., Tremblay, S. E., et al. 2015b, *ApJ*, 813, 18
- Stubbs, T. J., Glenar, D. A., Colaprete, A., & Richard, D. T. 2010, *Planet. Space Sci.*, 58, 830
- Sun, G., & Furlanetto, S. R. 2016, *MNRAS*, 460, 417
- Switzer, E. R., & Liu, A. 2014, *ApJ*, 793, 102
- Vedantham, H. K., & Koopmans, L. V. E. 2015, *MNRAS*, 453, 925
- Vedantham, H. K., Koopmans, L. V. E., de Bruyn, A. G., et al. 2014, *MNRAS*, 437, 1056
- , 2015, *MNRAS*, 450, 2291
- Veitch, J., Raymond, V., Farr, B., et al. 2015, *Phys. Rev. D*, 91, 042003
- Voytek, T. C., Natarajan, A., Jáuregui García, J. M., Peterson, J. B., & López-Cruz, O. 2014, *ApJ*, 782, L9
- Wouthuysen, S. A. 1952, *AJ*, 57, 31
- Zarka, P. 2004, in *Astronomical Society of the Pacific Conference Series*, Vol. 321, *Extrasolar Planets: Today and Tomorrow*, ed. J. Beaulieu, A. Lecavelier Des Etangs, & C. Terquem, 160
- Zheng, H., Tegmark, M., Dillon, J. S., et al. 2017, *MNRAS*, 464, 3486